

Influence of target material impurities on physical results in relativistic heavy-ion collisions

D. Banaś, A. Kubala-Kukuś, M. Rybczyński^a, I. Stabrawa, and G. Stefanek

Institute of Physics, Jan Kochanowski University, 25-406 Kielce, Poland

Received: 3 September 2018 / Revised: 28 November 2018

Published online: 30 January 2019

© The Author(s) 2019. This article is published with open access at Springerlink.com

Abstract. This paper presents the studies on the influence of the target material impurities on physical observables measured in heavy-ion collisions collected by fixed target experiments. It mainly concerns the measurements of multiplicity fluctuations, which can be used in searches for the critical point of strongly interacting matter, *e.g.* in the NA61/SHINE fixed-target experiment at CERN SPS. The elemental composition of the targets used in the NA61/SHINE experiment was determined applying the wavelength dispersive X-ray fluorescence (WDXRF) technique. The influence of the measured target impurities on multiplicity distributions and scaled variance was estimated using simulated events. A multiplicity analysis technique which limits the influences coming from target impurities was proposed.

1 Introduction

It is a well-established fact that matter exists in different states. For strongly interacting matter described by quantum chromodynamics (QCD) at least three states are expected: normal nuclear matter, hadron gas and a system of deconfined quarks and gluons (quark gluon plasma (QGP)). The conjectured QCD phase diagram [1] is usually displayed in the two-dimensional diagram —temperature, T , *versus* baryon chemical potential, μ_B . QCD predicts that the phase transition between the hadronic phase and the QGP in the large μ_B region is of the first order [2,3]. More qualitative results come from lattice QCD calculations which show that, in the vicinity of $\mu_B = 0$, there is a smooth crossover transition between the two phases. Thus the critical point of strongly interacting matter is the end point of the first-order phase transition boundary in the phase diagram, at which the transition is of second order and one cannot distinguish between the two phases [4]. Unfortunately, the QCD predictions are, to a large extent, qualitative, as QCD phenomenology at finite temperature and baryon number is one of the least explored domains of the theory. Especially due to a sign problem at the finite μ_B region, it is difficult to precisely determine the location of the critical point or even prove its existence [5].

It is very important to explore the QCD phase structure and search for the critical point theoretically and experimentally. From the theoretical side, it is very difficult to precisely determine the location of the critical point due to its non-perturbative nature. Many QCD-based models have given different results for the location of the critical point [6]. Nevertheless, most of the models locate it close to the chemical freeze-out line in the SPS energy range ($5 < \sqrt{s_{NN}} < 17$ GeV, where $\sqrt{s_{NN}}$ is the center-of-mass energy per nucleon pair). Experimentally, one can investigate the onset of deconfinement and search for the critical point in ion collisions by a scan of a broad region of the QCD phase diagram. The scan is possible experimentally by varying the energy and the size of the colliding nuclei. Such scans with energy were performed by the NA49 experiment using central Pb+Pb collisions. The results from the NA49 experiment suggest that the onset of deconfinement can be indirectly observed in central Pb+Pb interactions at low SPS energy, $\sqrt{s_{NN}} \approx 7.6$ GeV [7].

It is worth to emphasize that the experimental search for the critical point of strongly interacting matter is challenging because of the rapid expansion of the hot and dense medium created in ion collisions. To achieve this goal one has to select sensitive observables and signatures of the critical point and one needs to understand non-critical contributions to the experimental observables. In addition, the freeze-out conditions of the matter created in ion collisions should be close enough to the boundary, such that the phase transition signal does not get diluted. A characteristic property of the second-order phase transition at the critical point is the divergence of the susceptibilities.

^a e-mail: maciej.rybczynski@ujk.edu.pl

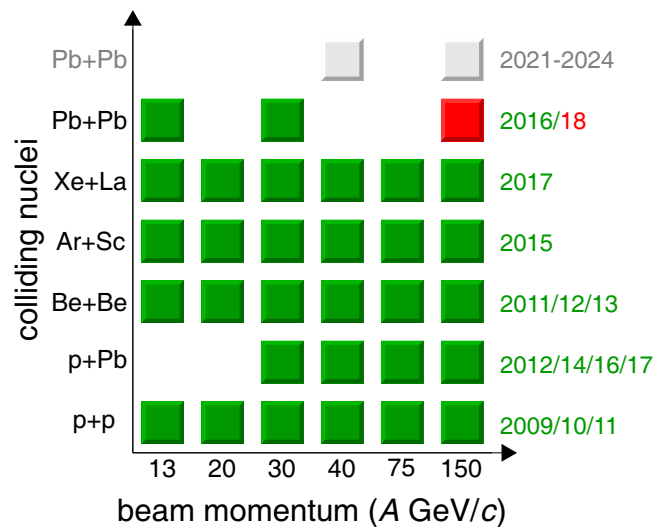


Fig. 1. The NA61/SHINE data samples for the programme of strong interactions. The recorded data are indicated in green, the approved future data taking in red, whereas the proposed extension for the period beyond 2020 in gray.

Consequently, important signals are large fluctuations, in particular an enhancement of fluctuations of multiplicity of produced particles and their transverse momenta [8] as well as fluctuations of conserved quantities, such as baryon, electric charge and strangeness number. The most efficient way to study the fluctuations of the system created in ion collision is to measure an observable event by event and to study the fluctuations over the events ensemble. In data analysis, one needs to apply various techniques to suppress background and to make precise measurements of fluctuations, which include the centrality bin width correction, the suppression of volume fluctuations and auto-correlations, and the efficiency correction. In fixed target experiments, like NA61/SHINE, there is an additional effect connected with target material impurities. Such impurities have an influence on fluctuation measurements by mixing collisions of projectile ion with various nuclei from the target. The effect is strongest in the case of measuring collisions of light ions with the target composed of light nuclei with impurities coming from heavy nuclei. A similar effect is expected in the opposite case, *i.e.* heavy-ion–heavy-nucleus collisions with impurities coming from light nuclei. It is obvious that the influence of impurities can be different for particles measured in different rapidity ranges.

The paper is organized as follows. In sect. 2 the NA61/SHINE experiment, the detector as well as collected data and targets are shortly described. The methodology of target impurities measurements by wavelength dispersive X-ray fluorescence (WDXRF) and the results are presented in sect. 3. The simulations done using the HIJING Monte Carlo model are described in sect. 4 together with the discussion of the impact of target impurities on multiplicity fluctuations measured by the NA61/SHINE experiment. Section 5 contains a brief description of a method allowing to estimate and to reduce the influence of target material impurities on the measured multiplicity distributions. Finally, sect. 6 contains the summary and conclusions.

2 The NA61/SHINE experiment

NA61/SHINE (SPS Heavy Ion and Neutrino Experiment) [9,10] is a multi-purpose fix-target experiment to study hadron production in hadron-proton, hadron-nucleus and nucleus-nucleus collisions at the CERN super proton synchrotron (SPS). The strong interaction programme of NA61/SHINE is devoted to the study of the onset of deconfinement and search for the critical point of hadronic matter. The NA49 experiment mainly studied hadron production in Pb+Pb interactions while the NA61/SHINE collects data at varying collision energy and size of the colliding systems. The programme was initiated in 2009 with p+p collisions. The data samples collected and planned for the future by the NA61/SHINE experiment within the strong interaction program are shown in fig. 1.

The NA61/SHINE experiment uses a large-acceptance hadron spectrometer located in the North Area Hall at the H2 beam-line. The main tracking devices of the spectrometer are large-volume time projection chambers (TPCs). Two of them, the vertex TPCs, are located in the magnetic fields of two super-conducting dipole magnets with maximum bending power of 9 Tm. The field in both magnets was lowered in proportion to the beam momentum in order to optimize the acceptance. The particles which go through the TPCs are almost entirely measured in the forward hemisphere (maximal range $-1.0 \lesssim y < y_{\text{beam}}$, y is the center-of-mass rapidity). Two time-of-flight (ToF) counters located on both sides of the beam just behind MTPCs supplement the NA61/SHINE experimental setup. They slightly extend the acceptance region towards midrapidity especially for charged kaons. Other sub-detectors of the NA61/SHINE setup like various beam counters and several other detectors were used in various configurations depending on colliding systems.

Table 1. The parameters of NA61/SHINE solid targets used for the program of strong interactions.

Target	Z	A	Thickness (cm)	Density (g/cm ³)	Interaction length (g/cm ²)
Be	4	9	1.2	1.850	77.8
Sc	21	45	0.6	2.985	123.9
La	57	139	0.3, 0.5	6.162	169.6
Pb	82	208	0.5	11.34	199.6

During data taking solid targets of ⁹Be, ⁴⁵Sc, ¹³⁹La, ²⁰⁸Pb and liquid hydrogen target have been used. The solid targets were mounted in the target holder. It has two possible positions for collecting events with target inserted and removed. The latter events were used for the correction of results for off-target interactions. The target parameters are presented in table 1.

The experiment measures the event-by-event fluctuations of particle multiplicities, their transverse momenta as well as particle composition fluctuations. In this paper we concentrate on the influence of target impurities on multiplicity fluctuations.

3 Measurement of impurities

3.1 Sample description

We analyzed the elemental composition of the beryllium (Be), scandium (Sc) and lanthanum (La) solid samples dedicated to use in the NA61/SHINE experiment. The samples were ordered from a professional manufacturer as high-purity materials (99.99%). The elemental analysis was performed using samples with a diameter of 40 mm which were prepared by the manufacturer for use with a commercial WDXRF spectrometer. The samples were delivered in a foil container and did not require an additional preparation procedure before the measurement. The lanthanum material was protected from oxidation by vacuum packaging. After unpacking the samples were placed immediately into the spectrometer and analysed.

3.2 Experimental setup and measurement conditions

The elemental composition of the studied samples was determined applying the wavelength dispersive X-ray fluorescence (WDXRF) technique. The physical basis of X-ray fluorescence analysis (XRF) is the photoelectric effect [11–13]. The X-ray primary beam emitted from a X-ray tube is directed onto the studied sample. X-ray photons ionize the sample atoms. The excited atoms decay to the ground state emitting characteristic X-ray radiation and photoelectrons (photoelectric effect) and/or electrons as a result of the Auger and Coster-Kronig processes. The XRF analytical technique is based on detection, qualitative and quantitative analysis of the characteristic X-rays. Additionally, in the WDXRF technique the wavelength dispersive mode of the characteristic X-ray detection is applied. In this detection method the non-monochromatic secondary X-ray beam emitted from the sample is directed onto the crystal on which the X-ray reflection takes place according to Bragg's law. A detector registers monochromatic radiation whose wavelength fulfills the Bragg's equation. Finally, the spectrum of the characteristic X-rays is measured, giving the qualitative and quantitative information about the elemental composition of the studied sample [14]. In the presented studies the WDXRF method was followed using the AXIOS spectrometer (Panalytical) equipped with an Rh-anode X-ray tube with maximum power of 2.4 kW [15]. The spectrum of the primary excitation X-ray beam is modified by different values of current and voltage of X-ray tube. Additionally, also primary beam filters can be applied: aluminum (200 μm), aluminum (750 μm), brass (100 μm) and brass (400 μm). The application of the filters results in the decrease of the radiation background in a different energy range improving the detection limit of the WDXRF technique. The use of the brass (400 μm) filter, due to the reduction of the K series lines of the X-ray tube, allows the determination of the rhodium concentration. The attenuation length of X-rays strongly depends on their energy and the atomic number of the elements in the sample. For example, for 30 keV X-rays the attenuation length is 33355 μm for Be, 785.3 μm for Sc and 157.5 μm for La [16]. The wavelength dispersive system of the spectrometer uses five crystals (LiF (200), Ge (111), PE (002), PX1 and LiF (220)) which were automatically selected during the measurements. The characteristic X-rays induced in the sample were diffracted on one of the crystals and measured by a flow proportional counter for optimal detection of elements up to Fe or a scintillation detector for heavier elements. The measurements were performed in vacuum. In order to cover the X-ray energy (wavelength) range of interest it was necessary to perform 11 scans by setting different current and voltage values for the X-ray tube and different diffraction crystal-detector configurations.

Table 2. Experimental conditions applied in WDXRF measurements: X-ray energy range, $K\alpha$ lines range of elements, $L\alpha$ lines range of elements, crystal, detector, primary beam filter, X-ray tube voltage and X-ray tube current.

Number of scan	Energy range (keV)	$K\alpha$ lines range	$L\alpha$ lines range	Crystal	Detector	Filter (μm)	Voltage (kV)	Current (mA)
1	27–36	Te-Ce	–	LiF220	Scint.	brass (100)	60	40
2	17–29	Mo-I	–	LiF220	Scint.	none	60	40
3	16–29	Nb-I	–	LiF200	Scint.	brass (400)	60	40
4	12–19	Kr-Tc	Ra-Am	LiF220	Scint.	Al (750)	60	40
5	8.5–13.5	Zn-Rb	Re-U	LiF220	Scint.	Al (200)	60	40
6	4.9–8.5	V-Cu	Pr-W	LiF220	Flow	none	50	48
7	3.24–5	K-V	In-Ce	LiF200	Flow	none	24	100
8	1.98–2.66	P-Cl	Zr-Ru	Ge111	Flow	none	24	100
9	1.68–1.80	Si-Si	Rb-Rb	PE002	Flow	none	24	100
10	1.478–1.542	Al-Al	Br-Br	PE002	Flow	none	24	100
11	0.5–1.4	O-Mg	V-Se	PX1	Flow	none	24	100

Table 3. Comparison of compound concentration in the certified reference solid sample with results obtained using AXIOS spectrometer.

Compound	Nominal concentration (%)	Experimental concentration (%)
$\text{Li}_2\text{B}_4\text{O}_7$	82.7	84.8
B_2O_3	2.5	–
CaO	2.80 (± 0.02)	2.79 (± 0.05)
Fe_2O_3	2.00 (± 0.02)	2.02 (± 0.04)
P_2O_5	4.5 (± 0.03)	4.46 (± 0.06)
SiO_2	4.00 (± 0.03)	4.12 (± 0.06)
SrO	0.50 (± 0.01)	0.47 (± 0.02)
ZnO	1.00 (± 0.01)	0.99 (± 0.03)

Detailed information on the measurement conditions is presented in table 2. The parameters of the scans (crystal, detector, primary beam filter, X-ray tube voltage and X-ray tube current) are optimized for the best detection limit for the analyzed element. The energy range of the characteristic X-rays registered by the spectrometer is in the range from 0.5 keV to 36 keV. The lightest element which can be detected with possible settings of the AXIOS spectrometer is oxygen (O).

The quantitative analysis of the spectra was performed with the AXIOS analytical program Omnian [17]. In this analysis the sample is assumed to be uniform. The Omnian package is available for the standardless analysis of all types of samples. Omnian includes advanced algorithms designed to profile known limitations inherent to XRF and includes spectral interference. The *dark matrix* correction provides better accuracy in cases where light elements such as C, H and O contribute to significant absorbance. In general, corrections which were involved in the Omnian quantitative analysis of the studied samples were as follows: finite thickness (correction where the sample was not infinitely thick for all measured energies) and Compton validation factor (the analysis of unmeasured matrix components by using the peak of the Compton-scattered primary X-ray beam). The certified reference material was always analyzed to validate the analytical procedure before the WDXRF measurement of an unknown sample. As an example the results of such an analysis are presented in table 3 for the reference solid sample (Panalytical). In the table the nominal value of the element concentrations are compared with the experimental values. It can be concluded that, in the range of the experimental uncertainties, a very good agreement was achieved.

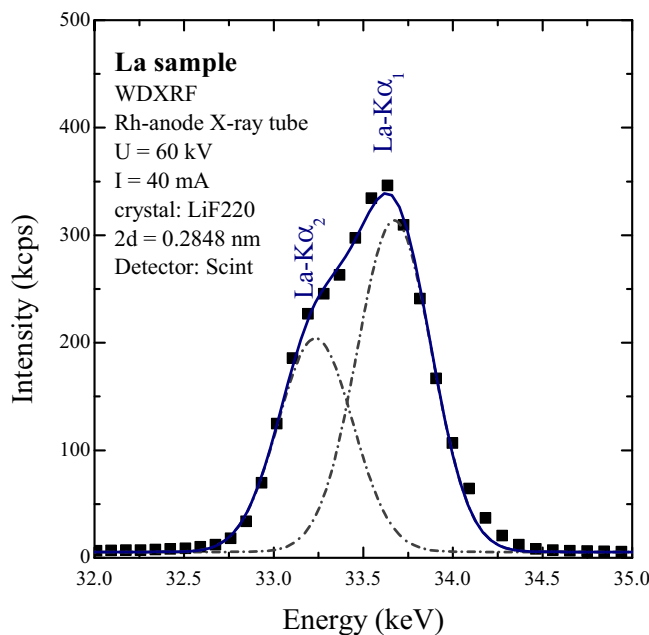


Fig. 2. Spectrum of the characteristic X-rays emitted from the La sample in the energy range of La-K α lines (La-K α_1 and La-K α_2). The spectrum was registered applying WDXRF technique with the experimental conditions given in the figure.

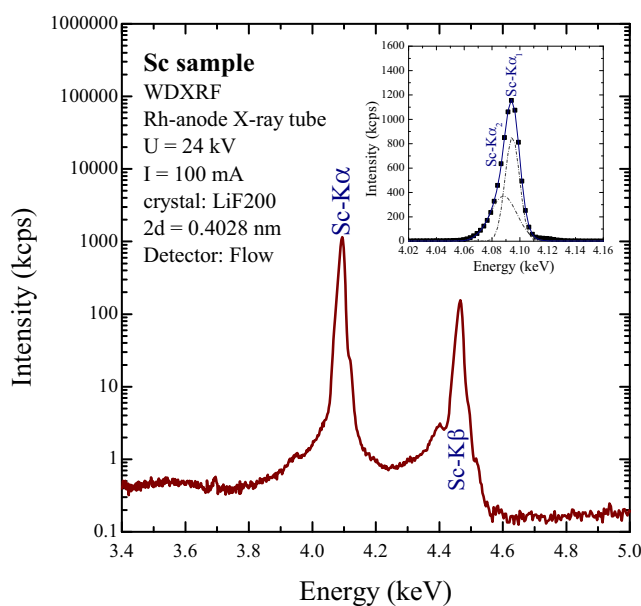


Fig. 3. Spectrum of the characteristic X-rays emitted from the Sc sample in the energy range of Sc-K α and Sc-K β lines (scan 7). Inside the fitted Sc-K α_1 and Sc-K α_2 lines are presented. Spectrum was registered applying WDXRF technique with the experimental conditions given in the figure.

Figure 2 shows the spectrum of the characteristic X-rays emitted from the La sample in the energy range from 32 keV to 35 keV, corresponding to the La-K α lines (La-K α_1 and La-K α_2). The experimental conditions are given inside the figure. The asymmetric shape of the line results from the overlapping of the La-K α_1 and La-K α_2 lines. The contribution of each line was fitted assuming Gaussian profile of the lines and constant full width of the distribution at half of maximum (FWHM). The position of the maximum of the La-K α_1 line was fitted as 33.673 keV and for La-K α_2 as 33.233 keV. The width of the each line was 0.490 keV.

The spectrum presented in fig. 3 was measured for the Sc sample in the range of Sc-K α and Sc-K β lines (on presented figure from 3.4 keV to 5 keV). The characteristic X-rays were excited by a primary X-ray beam from the X-ray tube operated with parameters 24 kV and 100 mA and the spectrum was registered using a LiF200 crystal and the flow detector. Inside the figure the Sc-K α_1 and Sc-K α_2 lines are presented. The fitted positions of the maxima of spectral lines are, respectively, 4.095 keV and 4.088 keV, and the FWHM is 0.015 keV, giving the energy resolution on the level 0.37%, which is relatively high resolution in spectroscopic applications.

Table 4. Full width at half maximum of the intensity (ΔE) for characteristic X-ray lines of the elements detected in the studied samples. The energy (E) of the X-ray lines, the crystal used in wavelength dispersive mode and energy resolution ($\Delta E/E$) are also presented.

Number of scan	Crystal	Line	Energy (E) (keV)	FWHM (ΔE) (keV)	$\Delta E/E$ (%)
11	PX1	O-K α	0.526	0.010	1.90
11	PX1	F-K α	0.679	0.012	1.77
10	PE002	Al-K α	1.489	0.002	0.13
9	PE002	Si-K α	1.743	0.004	0.23
8	Ge111	S-K α	2.311	0.006	0.26
7	LiF200	Sc-K α_2	4.088	0.015	0.37
7	LiF200	Sc-K α_1	4.095	0.015	0.37
6	LiF220	Fe-K α	6.407	0.025	0.39
6	LiF220	Ni-K α	7.481	0.036	0.48
2	LiF220	Mo-K α	17.527	0.143	0.82
1	LiF220	La-K α_2	33.233	0.490	1.47
1	LiF220	La-K α_1	33.673	0.490	1.46

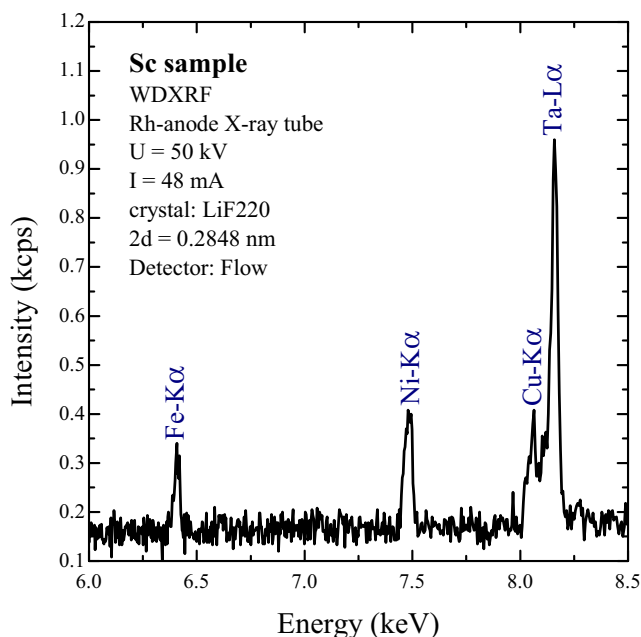


Fig. 4. Spectrum of the characteristic X-rays emitted from the Sc sample in the energy range from 6 keV to 8.5 keV. On the spectrum the Fe-K α , Ni-K α , Cu-K α and Ta-L α lines are marked coming from elements being the impurities of the Sc sample. The experimental conditions are also shown in the figure.

The energy resolution of the applied experimental setup was additionally systematically studied for different measurement conditions. FWHM of the intensity for characteristic X-ray lines of the elements detected in the studied samples are presented in table 4. For each crystal used in wavelength dispersive mode of X-ray detection the exemplary characteristic line is characterized by its energy in maximum, value of FWHM and energy resolution ($\Delta E/E$). It can be observed that energy resolution changes over a wide range, from 0.13% for crystal PE002 and energy 1.489 keV (Al-K α) to 1.9% for crystal PX1 and energy 0.526 keV (O-K α). The high-energy resolution allows for unambiguous identification of element intensity even for samples very rich in elemental composition, especially for light elements.

For the present study the Be, Sc, and La samples were analyzed in the context of the impurity concentrations. As an example, fig. 4 presents the spectrum of the characteristic X-rays emitted from the Sc sample in the energy range from 6 keV to 8.5 keV. On the spectrum the Fe-K α , Ni-K α , Cu-K α and Ta-L α lines are marked coming from elements being the impurities of the Sc sample.

Table 5. Measured elemental composition of Be sample determined using WDXRF technique. Since the lightest element possibly measured by the spectrometer using element characteristic X-rays is oxygen thus Be element was not detected directly. See text for details.

Element	Mass concentration (%)
Al	0.039 ± 0.008
Co	0.003 ± 0.002
Cu	0.008 ± 0.003
Fe	0.13 ± 0.014
Mg	0.05 ± 0.008
Mn	0.027 ± 0.005
S	0.003 ± 0.002
Ti	0.017 ± 0.004
V	0.002 ± 0.001
U	0.006 ± 0.002
W	0.002 ± 0.001

Table 6. Measured elemental composition of the Sc sample determined using WDXRF technique.

Element	Mass concentration (%)
Al	0.144 ± 0.011
Bi	0.028 ± 0.005
Ca	0.008 ± 0.003
Cl	0.011 ± 0.003
Cu	0.073 ± 0.008
Fe	0.130 ± 0.011
Mg	0.008 ± 0.003
Ni	0.027 ± 0.005
Pb	0.003 ± 0.002
S	0.006 ± 0.002
Sc	99.29 ± 1.00
Si	0.034 ± 0.006
Ta	0.065 ± 0.008
Ti	0.157 ± 0.012
W	0.017 ± 0.004
Y	0.002 ± 0.001

3.3 Results of the WDXRF measurements

Table 5 summarizes the composition of the impurities in the beryllium sample obtained using the WDXRF technique. The following elements were measured: Al, Co, Cu, Fe, Mg, Mn, S, Ti, V, U and W with mass concentration in the range from 0.002% (V and W) to 0.13% (Fe). The total concentration of admixed elements in beryllium sample is 0.287%. The unmeasured Be matrix compound was estimated using the peak of Compton-scattered primary X-ray beam.

In the case of the Sc sample, the following impurities were detected (table 6): Al, Bi, Ca, Cl, Cu, Fe, Mg, Ni, Pb, S, Si, Ta, Ti, W and Y. The lowest concentration is 0.002% (Y), the highest 0.157% (Ti) and the total concentration of the impurities is 0.71%.

Table 7. Measured elemental composition of La sample determined using WDXRF technique.

Element	Mass concentration (%)
Al	0.018 ± 0.004
Ba	0.035 ± 0.006
Ca	0.005 ± 0.002
Cl	0.006 ± 0.002
Fe	0.017 ± 0.004
La	99.73 ± 0.89
Mg	0.003 ± 0.002
Ni	0.002 ± 0.001
S	0.006 ± 0.002
Si	0.015 ± 0.004
Y	0.008 ± 0.003
Zn	0.158 ± 0.012

Table 7 summarizes the elemental composition of the La sample. In this sample the main impurity is Zn (0.158%). The concentration of the rest of the impurities: Al, Ba, Ca, Cl, Fe, Mg, Ni, S, Si, Y, is on a much lower level, from 0.002% to 0.035%. The total concentration of the admixed elements is 0.27%.

The experimental uncertainty of the impurity concentration is calculated from the error of the intensity of the characteristic X-ray and depends on the amount of the element. For the lowest concentration detected in the studied samples the relative uncertainty is on the level 50% while for the highest one it is about 1%.

The lowest value of given element concentration which can be detected, called low limit of detection (LLD), using WDXRF spectrometer depends on one hand on the experimental conditions and on the other hand on the type of the studied sample matrix, and can be calculated using the following formula:

$$LLD = \frac{3 \cdot C}{I_n} \cdot \sqrt{\frac{I_b}{t}}, \quad (1)$$

where C is the element concentration in the studied sample, I_n is the net intensity of the characteristic X-ray line, I_b is the background level under this line and t is the measurement dwell time. The background level is generated mainly by scattering of the X-ray radiation, both the primary beam and secondary characteristic radiation, in the sample. The scattering contribution depends on the energy of the X-rays and on the sample matrix, *i.e.* element composition in the sample and results in the different values of the element detection limit for as different samples as beryllium (Be), scandium (Sc) and lanthanum (La).

In the context of discussed properties of the interaction of the X-ray with matter, the detection limit was estimated using registered X-ray spectra, tables 5, 6, 7 and eq. (1), for all measured samples and for all detected impurities. For Be sample the best achieved detection limit is 3–4 ppm ($\mu\text{g/g}$) for U (U- $L\alpha_1$, scan number 4) and for S (S- $K\alpha$, scan 8). In case of the Sc sample, the lowest value of the LLD was on the level 10 ppm ($\mu\text{g/g}$) and it was observed for sulphur element (in general elements detected on the scans 2, 4 and 8). Finally, for the La sample, the lowest LLD value was on the level 15–20 ppm ($\mu\text{g/g}$) and it was observed for sulphur element (scan 8). The detection limits of the WDXRF spectrometer is on a sufficient level in the context of presented studies.

4 Impact on physical results

This section provides a brief description of our method to estimate the impact of impurities present in target materials on physics observables measured by the NA61/SHINE experiment. We focus on fluctuations of the number of charged particles produced in collisions. The magnitude of these fluctuations is often measured by the scaled variance of the multiplicity distribution, $\omega(N)$, defined as

$$\omega(N) = \frac{Var(N)}{\langle N \rangle}, \quad (2)$$

Table 8. Elemental composition of Be target as reported by the target producer.

Element	Mass concentration (%)
Be	99.48
C	0.15
Mg	0.08
Al	0.1
Si	0.06
Fe	0.13

where $Var(N)$ is the variance of the distribution and $\langle N \rangle$ is the average multiplicity. We also use the relative change of the value of scaled variance, Δ as a measure of the influence of impurities on multiplicity distributions. It is defined as

$$\Delta = \frac{|\omega_{\text{pure}}(N) - \omega_{\text{adm}}(N)|}{\omega_{\text{pure}}(N)} \cdot 100\%, \quad (3)$$

where $\omega_{\text{pure}}(N)$ is the scaled variance of multiplicity distribution of particles produced in collisions with target containing 100% of the nominal element (*pure target*) and $\omega_{\text{adm}}(N)$ is the one calculated for collisions with target containing impurities (*admixture target*).

4.1 Simulations

We analyzed the simulated multiplicity distributions of negatively charged particles generated in the collisions of ${}^7\text{Be} + {}^9\text{Be}$, ${}^{40}\text{Ar} + {}^{45}\text{Sc}$, ${}^{129}\text{Xe} + {}^{139}\text{La}$ and ${}^{208}\text{Pb} + {}^{208}\text{Pb}$ at energy measured in laboratory frame, $E_{\text{lab}} = 150$ GeV/nucleon ($\sqrt{s_{NN}} = 17$ GeV). Simulated events were generated using the HIJING Monte Carlo generator [18]. Two sets of simulated events were build. In both of them the projectile was the same as in the NA61/SHINE experiment, it means ${}^7\text{Be}$, ${}^{40}\text{Ar}$, ${}^{129}\text{Xe}$, and ${}^{208}\text{Pb}$. In the first set the target entirely consists of nominal elements ${}^9\text{Be}$, ${}^{45}\text{Sc}$, ${}^{139}\text{La}$, ${}^{208}\text{Pb}$ (*pure target*). The procedure of preparation of the second set is following. We generated the collisions of given projectile nucleus with all kinds of nuclei present in the *admixture target*, separately. Then we generated a set of collisions drawing events from simulated collisions with probabilities

$$p = \frac{N \cdot \sigma_{AB}}{\sum N \cdot \sigma_{AB}}, \quad (4)$$

where N is the number concentration¹ of a given element in the admixture target and $\sigma_{AB} = \pi \cdot R^2 (A^{1/3} + B^{1/3} - \delta)^2$ with $R = 1.4$ fm and $\delta = 1.12$ is the collision cross section of projectile nucleus with atomic mass A and target nucleus with atomic mass B [19, 20]. In the case of ${}^7\text{Be} + {}^9\text{Be}$ collisions, since the lightest element possibly measured by the AXIOS spectrometer is oxygen thus Be element was not detected and we assumed for simulations the mass concentration of ${}^9\text{Be}$ to be equal $100\% - 0.287\% = 99.713\%$. For ${}^7\text{Be} + {}^9\text{Be}$ interactions we also simulated events using information of concentrations of impurities reported by the target producer, see table 8. To prepare the admixture Pb target we assumed the number concentrations of nuclei in the target proportional to the abundances of stable Pb isotopes in the Earth's core [21]. Namely, we composed the admixture Pb target of 1.4% ${}^{204}\text{Pb}$, 24.1% of ${}^{206}\text{Pb}$, 22.1% of ${}^{207}\text{Pb}$, and 52.4% of ${}^{208}\text{Pb}$ nuclei.

For each simulated event the following quantities were registered: a) the number of projectile spectators; b) the multiplicity of negatively charged particles generated in the full kinematical acceptance; c) the multiplicity of negatively charged particles in the forward kinematical acceptance, defined by $y_\pi > 0$ (see footnote²). We selected the 5%³ most central collisions using the number of spectator nucleons from the projectile nucleus, N_S^{proj} as a measure of collisions centrality, similar to the definition used in the NA61/SHINE experiment [22]⁴. Each set of collisions contains

¹ Number concentrations of target elements were calculated with accordance to the measured mass concentrations of elements described in the previous sections.

² In the simulations we always assume the production of pions (with mass $m = 0.139$ GeV) and thus we used pion mass for the calculation of rapidity.

³ 10% in the case of ${}^{208}\text{Pb} + {}^{208}\text{Pb}$ collisions.

⁴ The NA61/SHINE experiment is equipped with the projectile spectator detector, PSD, which is an calorimeter measuring energy carried by the spectator nucleons from projectile, E_S^{proj} . The number of spectator nucleons can be estimated as $N_S^{\text{proj}} = E_S^{\text{proj}}/E_{\text{lab}}$, where E_{lab} is the energy carried by single spectator nucleon from projectile. Knowing N_S^{proj} it is straightforward to estimate the number of participating nucleons from projectile, $N_P^{\text{proj}} = A - N_S^{\text{proj}}$, where A denotes the atomic mass of projectile nucleus.

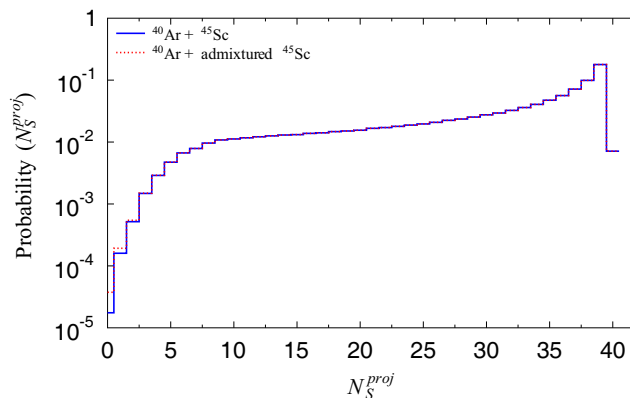


Fig. 5. Distribution of the number of projectile spectators, N_S^{proj} obtained in $^{40}\text{Ar} + ^{45}\text{Sc}$ collisions (solid line). Dotted line shows distribution simulated in the collisions of ^{40}Ar with admixed Sc target with elements composition taken from table 6.

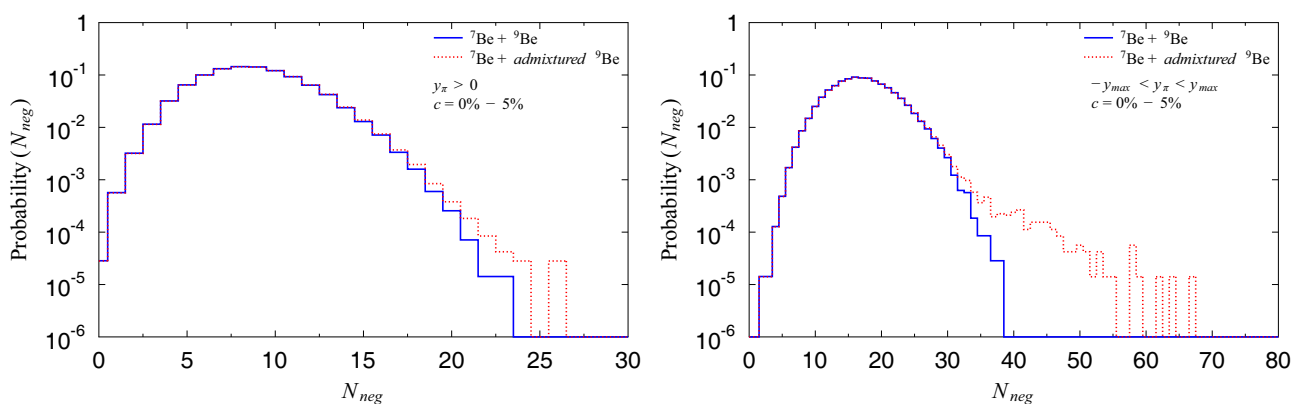


Fig. 6. Multiplicity distributions of negatively charged particles generated in $^7\text{Be} + ^9\text{Be}$ collisions in forward (left panel) and full (right panel) kinematical acceptances. Solid lines show distributions generated assuming target composed of pure ^9Be nuclei whereas with dotted line we present multiplicity distributions resulting from collisions of ^7Be nucleus with target composed of nuclei according to our WDXRF measurement, table 5.

$5 \cdot 10^5$ minimum bias events, thus also the number of central events is enough to limit statistical uncertainties. In fig. 5 we show the typical distribution of the number of projectile spectators obtained in $^{40}\text{Ar} + ^{45}\text{Sc}$ collisions. In fig. 5 we also present N_S^{proj} distribution obtained in the collisions of ^{40}Ar with Sc target admixed with elements composition taken from table 6. We observe only a very small influence of impurities in the admixed Sc target on the N_S^{proj} distribution (see first bins in fig. 5). The cut $N_S^{proj} \leq 10$ for the selection of 0%–5% centrality range is the same for collisions with pure and admixed targets because N_S^{proj} is the integer number and the difference between distributions in fig. 5 is very small.

4.2 Results of the simulations

In this subsection we present the results of the analysis of generated events. We focus on multiplicity distributions of negatively charged particles. Figure 6 shows multiplicity distributions of negatively charged particles generated in $^7\text{Be} + ^9\text{Be}$ collisions in forward and full kinematical acceptances⁵. Solid lines show distributions generated assuming target composed of pure ^9Be nuclei whereas the dotted line represents multiplicity distributions resulting from collisions of ^7Be nuclei with a target composed of nuclei according to our WDXRF measurement, table 5. In the case of collisions with admixed target we note substantial right-hand side tails in both distributions, of particles produced in forward as well as in full kinematical acceptance. The origin of these tails is mainly from the presence of heavy nuclei (V, U, W) in the target. It is important to note that the selection of the 5% of most central collisions favors collisions of ^7Be with heavier nuclei in the target and, hence, increases the relative contribution of different nuclei present in target material to the observed multiplicity distribution. So, in the centrality selected events there is a different contribution of target nuclei than in the target material. The relative change of scaled variance in $^7\text{Be} + ^9\text{Be}$ collisions is $\Delta = 2.2\%$ and $\Delta = 11.5\%$ for forward and full kinematical acceptances, respectively.

⁵ The symbol y_{\max} indicated in fig. 6 and the following plots describe the maximal, kinematically available value of rapidity.

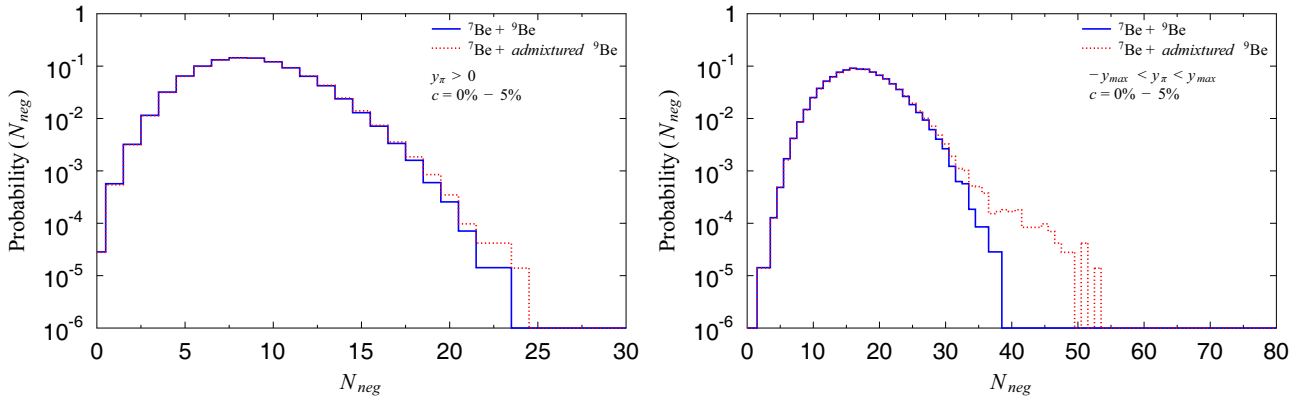


Fig. 7. The same as in fig. 6 but the target was composed of nuclei according to information reported by target producer, see table 8.

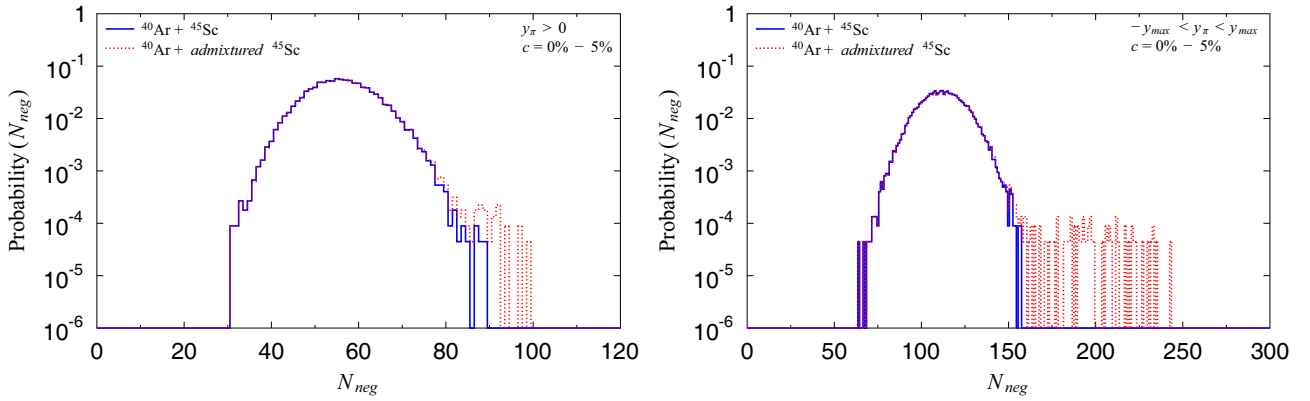


Fig. 8. The same as in fig. 6 but for $^{40}\text{Ar} + ^{45}\text{Sc}$ collisions. Admixed Sc target was composed of nuclei according to our WDXRF measurement, see table 6.

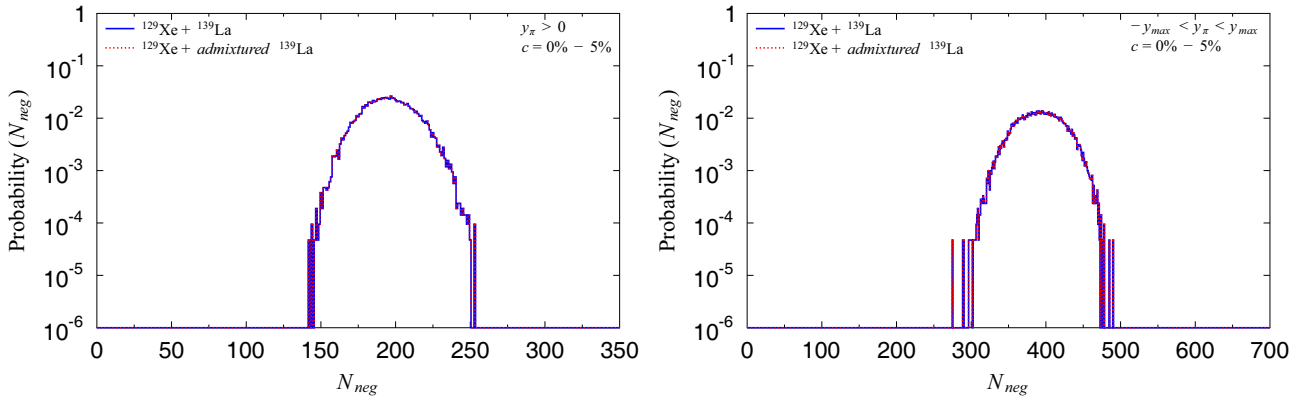


Fig. 9. The same as in fig. 6 but for $^{129}\text{Xe} + ^{139}\text{La}$ collisions. Admixed La target was composed of nuclei according to our WDXRF measurement, see table 7.

Figure 7 presents results similar to those in fig. 6 but obtained for the Be target elemental composition reported by the target producer. Similarly, like in fig. 6, there are also right-hand side tails in the distributions coming from the collisions with heavy nuclei in admixed target. Here, the size of the tails is smaller due to the different composition of target elements, in particular lack of very heavy elements, see table 8. In this case the relative change of scaled variance is equal to 1.4% and 8.7% for forward and full kinematical acceptances, respectively.

Figures 8 and 9 contain multiplicity distributions of negatively charged particles generated in the collisions of $^{40}\text{Ar} + ^{45}\text{Sc}$ and $^{129}\text{Xe} + ^{139}\text{La}$. For $^{40}\text{Ar} + ^{45}\text{Sc}$ collisions we also observe long tails in the distributions and the influence of target impurities are even larger than in the case of $^7\text{Be} + ^9\text{Be}$ collisions. The relative change of scaled variance in $^{40}\text{Ar} + ^{45}\text{Sc}$ collisions is $\Delta = 3.9\%$ and $\Delta = 16.4\%$ for forward and full kinematical acceptances, respectively.

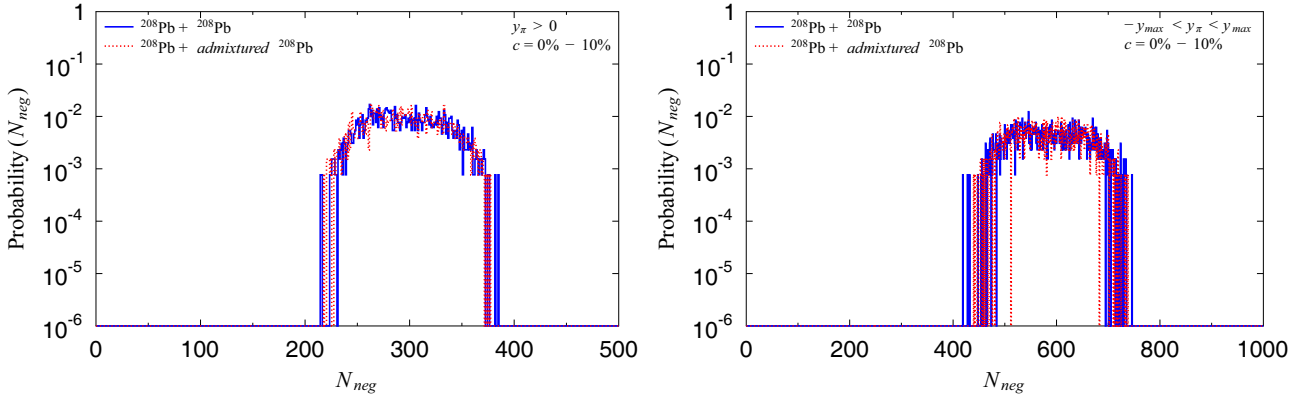


Fig. 10. Multiplicity distributions of negatively charged particles, generated in $^{208}\text{Pb} + ^{208}\text{Pb}$ collisions in forward (left panel) and full (right panel) kinematical acceptances. Full lines show distributions generated assuming target composed of pure ^{208}Pb nuclei whereas using dotted line we present multiplicity distributions coming from collisions with target composed of nuclei proportional to the abundances of stable Pb isotopes in the Earth's core.

Table 9. Average multiplicity of negatively charged particles and corresponding scaled variance of multiplicity distribution of particles generated in forward kinematical acceptance.

Colliding system	$\langle N_{\text{neg}} \rangle$	$\omega(N_{\text{neg}})$
$^7\text{Be} + ^9\text{Be}$	8.74 ± 0.01	0.864 ± 0.005
$^7\text{Be} + \text{admix. } ^9\text{Be}$ [Producer]	8.79 ± 0.01	0.876 ± 0.005
$^7\text{Be} + \text{admix. } ^9\text{Be}$ [WDXRF]	8.78 ± 0.01	0.883 ± 0.005
$^{40}\text{Ar} + ^{45}\text{Sc}$	56.02 ± 0.05	0.92 ± 0.01
$^{40}\text{Ar} + \text{admix. } ^{45}\text{Sc}$	56.11 ± 0.05	0.956 ± 0.009
$^{129}\text{Xe} + ^{139}\text{La}$	195.5 ± 0.1	1.3 ± 0.012
$^{129}\text{Xe} + \text{admix. } ^{139}\text{La}$	195.5 ± 0.1	1.3 ± 0.012
$^{208}\text{Pb} + ^{208}\text{Pb}$	296.0 ± 0.2	3.8 ± 0.05
$^{208}\text{Pb} + \text{admix. } ^{208}\text{Pb}$	295.4 ± 0.2	3.8 ± 0.05

The presence of tantalum and tungsten nuclei in the Sc target is mostly responsible for the asymmetric widening of multiplicity distributions. In contrast, for $^{129}\text{Xe} + ^{139}\text{La}$ collisions there is no influence of impurities for the analyzed multiplicity distributions. As one can deduce from fig. 9 the relative change of the value of scaled variance in $^{129}\text{Xe} + ^{139}\text{La}$ collisions is $\Delta \approx 0.0\%$ for both forward and full kinematical acceptances. Note that the presence of impurities with atomic mass lower than dominating element in the sample does not affect multiplicity distributions mainly due to the selection of 5% of most central events.

Figure 10 shows multiplicity distributions of particles generated in 10% most central events of $^{208}\text{Pb} + ^{208}\text{Pb}$ collisions. Here for the simulation of admixed target we assumed the presence of stable Pb isotopes proportional to their abundances in the Earth's core [21], as described in subsect. 4.1. We do not see any substantial influence of Pb isotopes for discussed multiplicity distributions. The relative change of the value of scaled variance in Pb+Pb collisions is, $\Delta \approx 0.0\%$ and $\Delta = 2.8\%$ for forward and full kinematical acceptances, respectively. We also performed similar simulations for lower energy, $E_{\text{lab}} = 40 \text{ GeV/nucleon}$ ($\sqrt{s_{NN}} = 8.8 \text{ GeV}$) with very similar results as for the collisions at $E_{\text{lab}} = 150 \text{ GeV/nucleon}$.

The results are summarized in tables 9 and 10 where we present numerical values of average multiplicity and corresponding scaled variance of presented multiplicity distributions in forward and full kinematical acceptances, respectively.

Table 10. Average multiplicity of negatively charged particles and corresponding scaled variance of multiplicity distribution of particles generated in full kinematical acceptance.

Colliding system	$\langle N_{\text{neg}} \rangle$	$\omega(N_{\text{neg}})$
${}^7\text{Be} + {}^9\text{Be}$	17.18 ± 0.02	1.139 ± 0.006
${}^7\text{Be} + \text{admix. } {}^9\text{Be}$ [Producer]	17.35 ± 0.02	1.238 ± 0.006
${}^7\text{Be} + \text{admix. } {}^9\text{Be}$ [WDXRF]	17.33 ± 0.02	1.27 ± 0.006
${}^{40}\text{Ar} + {}^{45}\text{Sc}$	112.1 ± 0.08	1.295 ± 0.012
${}^{40}\text{Ar} + \text{admix. } {}^{45}\text{Sc}$	112.45 ± 0.09	1.507 ± 0.014
${}^{129}\text{Xe} + {}^{139}\text{La}$	392.1 ± 0.2	2.08 ± 0.02
${}^{129}\text{Xe} + \text{admix. } {}^{139}\text{La}$	392.1 ± 0.2	2.08 ± 0.02
${}^{208}\text{Pb} + {}^{208}\text{Pb}$	585.6 ± 0.4	7.3 ± 0.04
${}^{208}\text{Pb} + \text{admix. } {}^{208}\text{Pb}$	584.0 ± 0.4	7.1 ± 0.04

5 The method of target impurities influence reduction

This section describes the analysis method which can be used to estimate and reduce the influence of unwanted collisions caused by the target material impurities.

Let $P(N)$ be the probability distribution function of multiplicity N . Using $P(N)$ one can define a function $g(N)$ which satisfies recurrence relation

$$g(N) = \frac{(N+1)P(N+1)}{P(N)}. \quad (5)$$

Different functions $g(N)$ describe different multiplicity distributions. For $g(N) = a = \text{const}$ the corresponding $P(N)$ equals

$$P(N) = \frac{a^N}{N!} \exp(-a), \quad (6)$$

which is the Poisson distribution with the average value $\langle N \rangle = a$. If $g(N) = a + b \cdot N$ then

$$P(N) = \frac{k(k+1)\dots(k+N-1)}{N!} \left(\frac{\langle N \rangle/k}{1 + \langle N \rangle/k} \right)^N \frac{1}{(1 + \langle N \rangle/k)^k} \quad (7)$$

is a well known negative binomial distribution with $\langle N \rangle$ being average multiplicity and parameter $k = a/b$. In the simplest case: $a = b$ (what leads to $k = 1$) one gets

$$g(N) = \frac{\langle N \rangle}{\langle N \rangle + 1} (N + 1), \quad (8)$$

which is commonly known as the Bose-Einstein enhancement or stimulated emission. Note that for the case of negative binomial distribution, the scaled variance of the multiplicity distribution may be expressed as

$$\omega(N) - 1 = \frac{\langle N \rangle}{k} = \frac{b\langle N \rangle}{a}. \quad (9)$$

As an example, in fig. 11, we present the results obtained for ${}^{40}\text{Ar} + {}^{45}\text{Sc}$ collisions. The linear functions $g(N_{\text{neg}}) = a + b \cdot N_{\text{neg}}$ with the coefficients $a = 60$, $b = -0.08$ and $a = 90$, $b = 0.235$ for forward and full kinematical acceptances, respectively, describe well the results coming from the *pure* ${}^{40}\text{Ar} + {}^{45}\text{Sc}$ collisions. Red points on the right-hand sides of the plots showing a substantial deviation from the linear dependence correspond to the tails of the multiplicity distributions resulting from ${}^{40}\text{Ar}$ collisions with impurities in the Sc target. In order to avoid the influence of the long, unwanted tails of the multiplicity distributions one can cut them starting from multiplicities where the values of recurrence function $g(N)$ occurs start to deviate from the linear dependence.

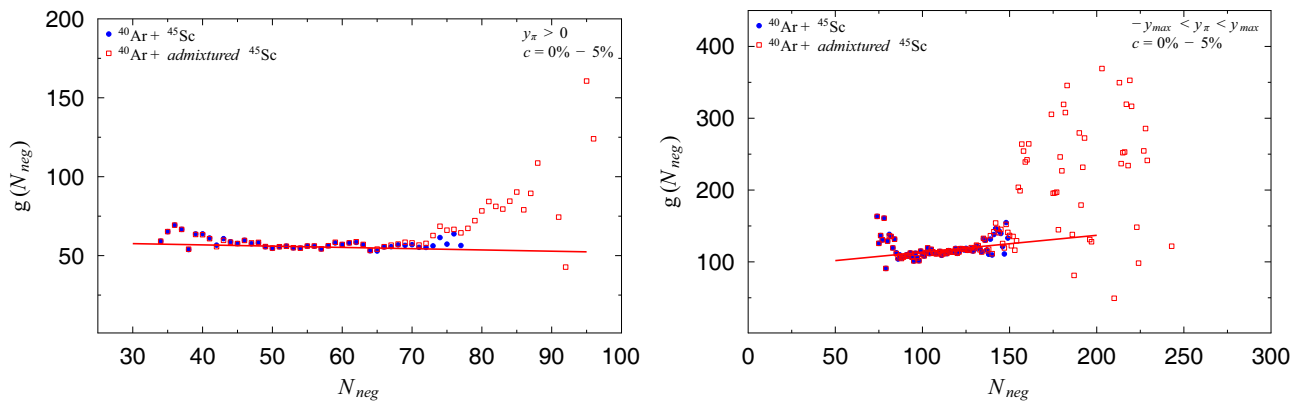


Fig. 11. Recurrence functions $g(N_{neg})$ calculated from multiplicity distributions of negatively charged particles generated in $^{40}\text{Ar} + ^{45}\text{Sc}$ collisions in forward (left panel) and full (right panel) kinematical acceptances. Full circles show results for collisions with target composed of pure ^{45}Sc nuclei whereas with empty squares we present results from collisions of ^{40}Ar nucleus with target composed of nuclei according to our WDXRF measurement, table 6. The full lines correspond to the linear functions: $g(N_{neg}) = 60 - 0.08 \cdot N_{neg}$ and $g(N_{neg}) = 90 + 0.235 \cdot N_{neg}$ for forward and full kinematical acceptances, respectively.

6 Conclusions

Distributions of charged particles are observables closely connected with the search of critical point of strongly interacting matter already performed in many existing high-energy physics experiments. Part of them, like NA61/SHINE, use fixed-target and dedicated detectors. We analyzed the influence of target material impurities on multiplicity distributions of charged particles produced in most central relativistic heavy-ion collisions using HIJING event generator. The following systems were studied: $^7\text{Be} + ^9\text{Be}$, $^{40}\text{Ar} + ^{45}\text{Sc}$, $^{129}\text{Xe} + ^{139}\text{La}$ and $^{208}\text{Pb} + ^{208}\text{Pb}$ at energies available at CERN SPS. The collisions of considered systems was already registered by the NA61/SHINE experiment at CERN SPS energies. The element compositions of the NA61/SHINE target samples were determined applying wavelength dispersive X-ray fluorescence (WDXRF) technique. Our main results are as follows:

- In the case of 5% most central $^7\text{Be} + ^9\text{Be}$ interactions we found a substantial influence of target impurities on multiplicity distributions of negatively charged particles produced in both forward and full kinematical acceptances. The presence of long tails in the multiplicity distributions is caused by the contamination of target material with heavy nuclei including uranium. Selection of central collisions favors heavier nuclei in target and changes the contribution of different nuclei present in target material to the observed multiplicity distributions.
- In 5% most central $^{40}\text{Ar} + ^{45}\text{Sc}$ collisions we found a large impact of target admixtures on analyzed multiplicity distributions. The relative change of scaled variance is $\Delta = 3.9\%$ and $\Delta = 16.4\%$ for forward and full kinematical acceptances, respectively. We identified Tantalum and Tungsten nuclei present abundantly in the ^{45}Sc target which are mostly responsible for the widening of multiplicity distributions.
- However, in contrast, in the case of central $^{129}\text{Xe} + ^{139}\text{La}$ collisions there is no influence of measured target impurities on observed multiplicity distributions. In the La target there is no measured elements heavier than ^{139}La and the selection of 5% of most central events practically excludes the contribution of particles produced in collisions of ^{129}Xe with lighter elements to observed multiplicity distributions.
- The influence of stable Pb isotopes possibly present in the Pb target on the observed multiplicity distributions was checked. Multiplicity distributions of particles produced in $^{208}\text{Pb} + ^{208}\text{Pb}$ collisions were compared with those produced in collisions of ^{208}Pb nuclei with the target for which we assumed the presence of isotopes proportional to their abundances in the Earth's core. We report no substantial differences between analyzed multiplicity distributions prepared from different sets of collisions.
- We proposed the method to estimate and reduce the influence of target impurities on multiplicity analysis and scaled variance calculation.

This work was motivated by the CERN NA61/SHINE experiment programme of study of phase diagram of strongly interacting matter. We thank A. Aduszkiewicz, M. Gaździcki and Z. Włodarczyk for useful discussions. The equipment was purchased thanks to the financial support of the European Regional Development Fund in the framework of the Polish Innovative Economy Operational Program (contract no. WNP-POIG.02.02.00-26-023/08) and the Development of Eastern Poland Program (contract no. POPW.01.01.00-26-013/09-04). The numerical simulations were carried out in laboratories created under the project “Development of research base of specialized laboratories of public universities in Swietokrzyskie region”, POIG 02.2.00-26-023/08, 19 May 2009. MR was supported by the Polish National Science Centre (NCN) grant 2016/23/B/ST2/00692.

Open Access This is an open access article distributed under the terms of the Creative Commons Attribution License (<http://creativecommons.org/licenses/by/4.0>), which permits unrestricted use, distribution, and reproduction in any medium, provided the original work is properly cited.

References

1. S. Gupta, X. Luo, B. Mohanty, H.G. Ritter, N. Xu, *Science* **332**, 1525 (2011).
2. P. de Forcrand, O. Philipsen, *Nucl. Phys. B* **642**, 290 (2002).
3. G. Endrodi, Z. Fodor, S.D. Katz, K.K. Szabo, *JHEP* **04**, 001 (2011).
4. Z. Fodor, S.D. Katz, *JHEP* **04**, 050 (2004).
5. R.V. Gavai, *Pramana* **84**, 757 (2015).
6. M.A. Stephanov, *Int. J. Mod. Phys. A* **20**, 4387 (2005).
7. NA49 Collaboration (C. Alt *et al.*), *Phys. Rev. C* **77**, 024903 (2008).
8. M.A. Stephanov, K. Rajagopal, E.V. Shuryak, *Phys. Rev. D* **60**, 114028 (1999).
9. NA49-future Collaboration (N. Antoniou *et al.*), CERN-SPSC-2006-034, CERN-SPSC-P-330.
10. NA61 Collaboration (N. Abgrall *et al.*), CERN-SPSC-2008-018, CERN-SPSC-SR-033.
11. B.K. Agarwal, *X-ray Spectroscopy* (Springer-Verlag, Berlin, Heidelberg, 1991).
12. R. Van Grieken, A. Markowicz (Editors), *Handbook of X-ray Spectrometry* (Marcel Dekker, New York, 1993).
13. B. Dziunikowski, *Energy Dispersive X-Ray Fluorescence Analysis* (Państwowe Wydawnictwo Naukowe PWN, Warszawa, 1989).
14. J.P. Willis, A.R. Duncan, *Understanding XRF Spectrometry* (PANalytical B.V., Almelo, 2008).
15. <http://www.panalytical.com>.
16. <http://henke.lbl.gov>.
17. Axios, *SuperQ5 Reference Manual* (PANalytical B.V., Almelo, 2005).
18. M. Gyulassy, X.N. Wang, *Comput. Phys. Commun.* **83**, 307 (1994) nucl-th/9502021.
19. H.L. Bradt, B. Peters, *Phys. Rev.* **77**, 54 (1950).
20. G.D. Westfall, L.W. Wilson, P.J. Lindstrom, H.J. Crawford, D.E. Greiner, H.H. Heckman, *Phys. Rev. C* **19**, 1309 (1979).
21. J. de Laeter, J. Boehlke, P. De Bièvre *et al.*, *Pure Appl. Chem.* **75**, 683 (2009).
22. NA61 Collaboration (N. Abgrall *et al.*), *JINST* **9**, P06005 (2014) arXiv:1401.4699 [physics.ins-det].